Catal Lett (2012) 142:275–281
DOI 10.1007/s10562-011-0748-2

Nanocasting Synthesis of Mesostructured Co_3O_4 via a Supercritical CO_2 Deposition Method and the Catalytic Performance for CO Oxidation

Yanhua Zhang · Aiqin Wang · Yanqiang Huang · Qinqin Xu · Jianzhong Yin · Tao Zhang

Received: 15 September 2011 / Accepted: 16 November 2011 / Published online: 30 November 2011

Abstract We demonstrate a supercritical CO_2 ($scCO_2$) deposition method to synthesize mesostructured Co_3O_4 with crystalline walls using SBA-15 as the hard template. By variation of the $scCO_2$ pressure, randomly organized nanorods or a highly ordered mesoporous structure of Co_3O_4 is obtained after only one filling operation. The catalytic tests show that the randomly organized Co_3O_4 nanorods display excellent activity for CO oxidation with the complete conversion of CO even at room temperature, while neither the ordered mesoporous nor bulk Co_3O_4 is active at this low-temperature, demonstrating the important role of Co_3O_4 morphology in catalysis.

Keywords Mesoporous · Nanocasting · Co_3O_4 · Supercritical CO_2 · CO oxidation

1 Introduction

Transition metal oxides are a kind of important materials as catalysts or catalyst supports due to their unique redox properties [1, 2]. The catalytic performance of a transition metal oxide is not only dependent on its intrinsic electronic properties, but also strongly dependent on its crystal size and morphology. It is therefore of great interest to synthesize a variety of transition metal oxides with controllable crystal size and morphology [3, 4].

Cobalt oxide (Co_3O_4) is a typical transition metal oxide and is widely used in catalytic oxidation reactions [5–9]. However, bulk Co_3O_4 usually possesses a low surface area (~ 20 m^2/g) which is unfavorable to its applications either as a catalyst or as a catalyst support. Mesoporous Co_3O_4, on the other hand, possessing the advantages of large surface areas (>100 m^2/g) and tunable pore structures, has attracted much attention both in material science and in catalysis [10–15]. It has been shown that mesoporous Co_3O_4 exhibited much better catalytic performance than bulk Co_3O_4 in CO oxidation [15, 16] and in VOC removal [13].

Nanocasting is a very effective method to produce mesoporous Co_3O_4, in which mesoporous silica or carbon serves as a hard template and its pores are infiltrated with precursors of Co_3O_4 followed by calcination and removal of the hard template [17–19]. The key to the success of nanocasting is the complete filling of the mesopores because partial or insufficient loading of precursors inside mesopores is very likely to result in replicas with disordered pore structures. However, due to the surface tension of the solvent, it usually requires several times of repetitive infiltration to accomplish the complete filling [18, 19]. In particular, when the hard template has long 1D channels, e.g., SBA-15, the infiltration of the mesopores will become more difficult.

Supercritical CO_2 ($scCO_2$) is a green and easily available solvent. The low viscosity, zero surface tension, high diffusivity, as well as good dissolving capability of $scCO_2$ make it an ideal medium to carry the target compounds into 1D long channels of the mesoporous silica [20, 21]. In the

Y. Zhang · A. Wang · Y. Huang · T. Zhang (✉)
State Key Laboratory of Catalysis, Dalian Institute of Chemical Physics, Chinese Academy of Sciences, Dalian 116023, China
e-mail: taozhang@dicp.ac.cn

Y. Zhang
Graduate School of the Chinese Academy of Sciences, Beijing 100049, China

Q. Xu · J. Yin
School of Chemical Machinery, Dalian University of Technology, Dalian 116024, China

present work, we use $scCO_2$ as the solvent and ethanol as a co-solvent to carry $Co(NO_3)_2$ into the channels of SBA-15 (hereafter the process is called as $scCO_2$ deposition). By variation of the $scCO_2$ pressure, the pore filling percents can be effectively tuned, thus different morphologies of the resultant Co_3O_4 replicas are obtained. Finally, the catalytic activities of the mesoporous Co_3O_4 with different morphologies are evaluated for low-temperature CO oxidation.

2 Experimental

2.1 Synthesis of Mesoporous Co_3O_4

SBA-15 was synthesized according to the reported method [22] and then calcined at 550 °C in air for use as the hard template. The setup for $scCO_2$ deposition is similar to those reported in literature [21]. For the synthesis of mesoporous Co_3O_4, 5 mL of a certain concentration of $Co(NO_3)_2$ ethanol solution was put in a stainless steel autoclave (with a volume of 40 mL), while 0.5 g of SBA-15 powder was placed in a filter-paper bag which was fixed in the upper part of the autoclave so that the template was not in contact with the precursor solution. The autoclave was charged with CO_2 until the desired pressure, and the ethanol solution was stirred for 0.5 h at 50 °C at this pressure. Afterwards, the autoclave was depressurized slowly (0.167 MPa/min) until ambient pressure, and then the impregnated SBA-15 (denoted as Co_3O_4@SBA-15) was calcinated at 550 °C in air for 5 h. The silica template was finally removed by etching with a 2 M hot NaOH solution and this procedure was repeated for three times. The template-free sample was washed with distilled water, centrifugated and dried at 60 °C overnight.

For comparison, bulk Co_3O_4 was prepared by a precipitation process at 60 °C using $Co(NO_3)_2 \bullet 6H_2O$ as the precursor and Na_2CO_3 as a precipitator [7]. After recovery, the precipitate was calcined at 550 °C for 5 h, and denoted as Co_3O_4-bulk.

2.2 Characterizations

X-ray diffraction (XRD) patterns were collected on a PW3040/60 X' Pert PRO (PANalytical) diffractometer equipped with a Cu Kα radiation source ($\lambda = 0.15432$ nm), operating at 40 kV and 40 mA. A continuous mode was used for collecting data at a scanning speed of 5°/min. TEM images and selected area electron diffraction (SAED) patterns were obtained on a JEOL 2000EX electronic micoroscope operating at 120 kV. The samples were prepared by dispersing the powders in ethanol and the dispersion was dropped on a carbon polymer supported on a copper grid. The high resolution transmission electron microscopy (HRTEM) images were obtained with Tecnai G^2 F30 S-Twin Transmission Electron Microscope, operating at 300 kV. Nitrogen adsorption–desorption measurements were performed at −196 °C with a Micromeritics ASAP2010 instrument. Prior to the measurements, the samples were degassed at 150 °C for 5 h. The specific surface areas were calculated with BET equation and the total pore volumes were obtained at a relative pressure (P/P_0) of 0.99. The pore sizes were determined from the desorption branches of the isotherms by Barrett–Joyner–Halenda (BJH) method. The residual silica contents of the resulting Co_3O_4 replicas were determined by inductively coupled plasma spectrometer (ICP-AES) on an IRIS Intrepid II XSP instrument (Thermo Electron Corporation). The temperature-programmed reductions with CO (CO-TPR) were carried out on an Auto Chem II 2920 automatic catalyst characterization system. 60 mg of a catalyst sample was loaded into a U-shape quartz reactor and pre-oxidized with air at 500 °C for 0.5 h. Then, after cooling to room temperature under He, the flowing gas was switched to a 5 vol% CO/He, and the sample was heated from 50 to 800 °C at a ramping rate of 10 °C/min.

2.3 Catalytic Activity Test

CO oxidation was used as a probe reaction for evaluating the catalytic activity of the mesoporous Co_3O_4. The reaction was carried out in a continuous fixed bed reactor at ambient pressure. Prior to the reaction, all the catalyst samples were pre-oxidized with O_2 (5 v/v%) in He at 500 °C for 0.5 h. After cooling to room temperature, a feed gas containing 1 vol% CO, 1 vol% O_2, and 98 vol% He was allowed to pass through 60 mg of a catalyst sample at a flow rate of 20 ml min^{-1} (corresponding to a space velocity of 20,000 ml h^{-1} g_{cat}^{-1}). The catalytic activity was evaluated in a temperature-increased mode; at each point the temperature was kept for 0.5 h. The inlet and outlet gas compositions were analyzed on-line by a gas chromatograph (HP 6890, TDX-01 column), and the CO conversion was calculated by the difference between inlet and outlet concentrations of CO.

3 Results and Discussion

One feature of $scCO_2$ fluid is that its physical properties such as density, viscosity, and solvation power are tunable by variation of the pressure. Thus, when $scCO_2$ is employed as the fluid to carry $Co(NO_3)_2$ precursor to the channels of SBA-15, it is expected that the change of $scCO_2$ pressure will bring about the variation of the Co loading and then the morphologies of Co_3O_4 replica. In this work, we select two pressures of $scCO_2$, 13 MPa and

23 MPa for the synthesis of mesoporous Co_3O_4, and the resultant materials are denoted as Co_3O_4-13 MPa and Co_3O_4-23 MPa, respectively. $ScCO_2$ at 13 MPa has a density of 0.590 g/cm^3 and viscosity of 52.47 μpa·s. At the higher pressure of 23 MPa, the density and viscosity increase to 0.798 g/cm^3 and 74.96 μpa·s, respectively. As a result, the solvation power of $scCO_2$ will be much stronger at the high pressure of 23 MPa [23]. First, we conducted the N_2-sorption experiment on the composites Co_3O_4@SBA-15-13 MPa and Co_3O_4@SBA-15-23 MPa. As shown in Table 1, in comparison with the parent SBA-15 hard template, distinct reduction of surface area and pore volume is observed for both composite samples, indicating a significant amount of Co_3O_4 has been deposited into the pores of SBA-15. In particular for the Co_3O_4@SBA-15-23 MPa, the surface area and pore volume decrease by ca. 70% than SBA-15. Nevertheless, the pore size decreases only to a minor extent after the deposition. This might be caused by the inhomogeneous infiltration, with a high degree of filling in some parts while little filling in other areas [11]. Based on the weight gain after the deposition, we can calculate the contents of Co_3O_4 in the composites to be 33 wt% for Co_3O_4@SBA-15-13 MPa and 62 wt% for Co_3O_4@SBA-15-23 MPa, which correspond to the pore filling percents of 9 and 29, respectively. Evidently, high pressure of $scCO_2$ is favorable to carry more precursors of cobalt nitrate precursor into the mesopores of SBA-15, which is in consistence with the enhanced solvation power of $scCO_2$ at a high pressure. It should be pointed out that the complete filling of the mesopores of SBA-15 template is not feasible because of a large mass loss during the decomposition of cobalt nitrate precursor. To evaluate if the pore filling percent at 23 MPa arrives at the threshold filling, we repeated the filling procedure twice at 13 MPa. The resultant composite (denoted as Co_3O_4@SBA-15-13 MPa-II) presents a further decreased surface area and pore volume (Table 1), very close to the sample of Co_3O_4@SBA-15-23 MPa. The pore filling percent after the two repetitive filling operations is calculated to be 25%, which is also close to the pore filling percent at 23 MPa. This result suggests that the pore filling at high pressures is so efficient that only one filling operation can achieve the threshold.

On the other hand, the loading of Co_3O_4 does not alter the N_2-sorption isotherm of SBA-15. As shown in Fig. 1, all the three composite materials show typical type IV isotherms and well defined hysteresis loops, indicating the ordered mesoporous structure is retained well even after the deposition of a significant amount of Co_3O_4 in the pores.

Figure 2 shows XRD patterns of the Co_3O_4 samples after removing the SBA-15 template. For the Co_3O_4-13 MPa, no any XRD peak can be observed in the low-angle region, suggesting a totally disordered mesostructure for this sample. In contrast, for the Co_3O_4-23 MPa, there are three well-resolved diffraction peaks which can be indexed as reflections of (100), (110) and (200) of *p6mm* hexagonal mesophase, indicating the formation of well-ordered hexagonal mesoporous structure similar to that of SBA-15. Evidently, high pressure of $scCO_2$ is favorable to the complete filling of the template pores with $Co(NO_3)_2$. When the $scCO_2$ deposition procedure was repeated twice at the pressure of 13 MPa, the resultant Co_3O_4 replica (denoted as Co_3O_4-13 MPa-II) showed low-angle XRD pattern very similar to that of Co_3O_4-23 MPa (not shown here). The wide-angle XRD patterns of the three samples are characteristic of cubic phase of Co_3O_4 (JCPDS card no.010761802), indicating that the mesoporous Co_3O_4 have highly crystalline walls. Moreover, compared with

Table 1 Textural parameters of SBA-15 template before and after loading of Co_3O_4 and the resultant mesoporous Co_3O_4 samples

Sample	S_{BET}[a] (m^2 g^{-1})	V_T[b] (cm^3 g^{-1})	D_p[c] (nm)
SBA-15	658	0.93	5.7
Co_3O_4@SBA-15-13 MPa	316	0.42	5.4
Co_3O_4@SBA-15-23 MPa	207	0.28	5.2
Co_3O_4@SBA-15-13 MPa-II	191	0.24	5.1
Co_3O_4-13 MPa	111	0.40	3.2, 23.3
Co_3O_4-23 MPa	101	0.22	3.6
Co_3O_4-13 MPa-II	102	0.30	3.2
Co_3O_4-bulk	18	–	–

[a] BET surface area

[b] Total pore volumes obtained at $P/P_0 = 0.99$

[c] Pore size determined from the desorption branches by BJH method

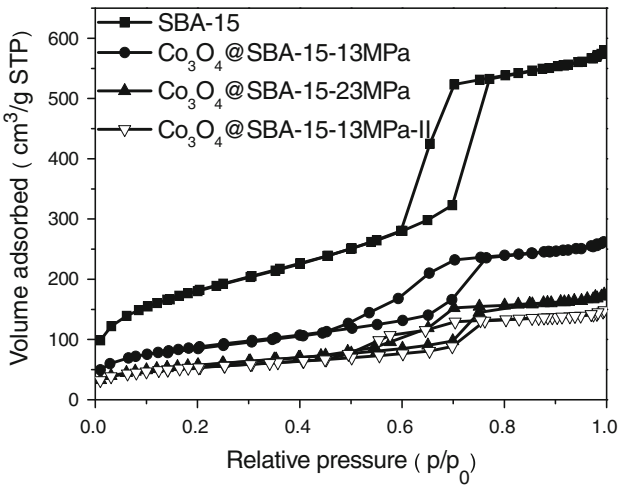

Fig. 1 Nitrogen physisorption isotherms of SBA-15 template before and after loading of Co_3O_4

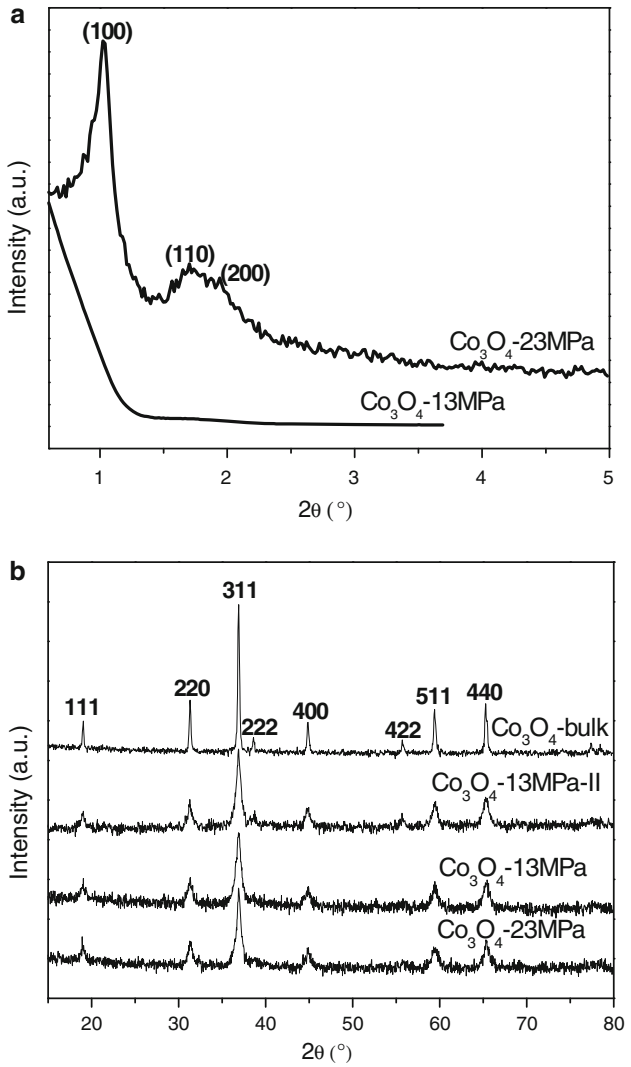

Fig. 2 XRD patterns of different Co_3O_4 samples in the low-angle (**a**) and wide-angle (**b**) regions

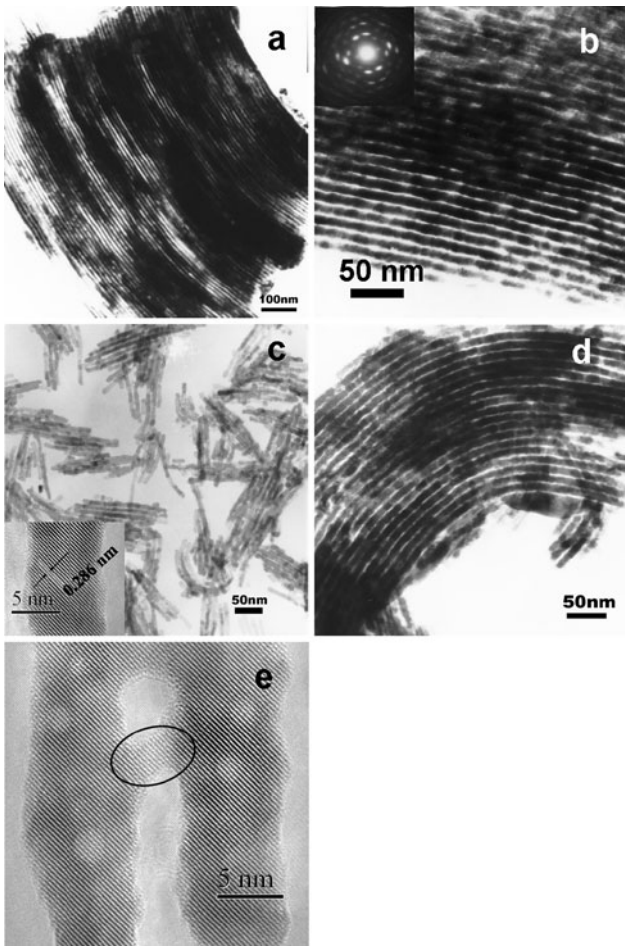

Fig. 3 TEM images of (**a**) Co_3O_4@SBA-15-23 MPa, (**b**) Co_3O_4-23 MPa, (**c**) Co_3O_4-13 MPa, (**d**) Co_3O_4-13 MPa-II and (**e**) HRTEM image of Co_3O_4-23 MPa. SAED image of Co_3O_4-23 MPa and HRTEM image of Co_3O_4-13 MPa are in the insets

bulk Co_3O_4, the three mesoporous samples present broader XRD peaks, suggesting much smaller crystal particles of these Co_3O_4 samples replicated from SBA-15. Estimation of the crystal sizes using Scherrer's formula on the (311) diffraction peak shows crystal sizes of 11 nm, 13 nm and 14 nm for Co_3O_4-13 MPa, Co_3O_4-13 MPa-II, and Co_3O_4-23 MPa, respectively. It is believed that the smaller crystal sizes of the mesoporous Co_3O_4 replica is ascribed to the confinement by the pore walls of the template [24].

The mesoporous structures of the samples are visually observed by transmission electron microscopy (TEM). Figure 3a shows a typical TEM image of Co_3O_4@SBA-15-23 MPa. It can be seen that most mesopores of the template are entirely filled with Co_3O_4 crystals (the dark areas) and there are no large Co_3O_4 particles growing outside the mesopores. In contrast, it was reported that the high cobalt nitrate concentration of 1.6 M or 3.2 M in conventional evaporation impregnation led to the formation of bulk cobalt oxide particles outside the pores of silica [18]. After removal of the silica template by etching with NaOH solution, mesoporous Co_3O_4 replica with well-ordered pore arrangement was obtained as indicated in Fig. 3b. The selected area electron diffraction (SAED) pattern from large areas shown in the inset is consisted of single spots, confirming the formation of highly crystalline walls. This is in agreement with the XRD results. On the other hand, for the Co_3O_4-13 MPa, nanorods with lengths of 100–200 nm and diameters of 5–9 nm are clearly observed (Fig. 3c), and these nanorods are randomly arranged and do not constitute any large domains with ordered structure. The high resolution transmission electron microscopy (HRTEM) reveals that the [220] crystal plane with a lattice space of 0.286 nm (inset in Fig. 3c) is predominantly exposed for this sample [4]. It seems that the diameters of Co_3O_4 nanorods are larger than the average pore size of SBA-15 (5.7 nm). Nevertheless, considering the

uncertainties both in the determination of the pore size and in the exact measurement of the rod diameters in the TEM, we can think the size of rods fits with the pore size of the template SBA-15. The similar phenomenon was also observed in the nanocasting synthesis of Co_3O_4 by other group [18]. The formation of randomly arranged nanorods is mainly caused by the incomplete filling of the template mesopores. When the deposition procedure was repeated twice at the $scCO_2$ pressure of 13 MPa, the resultant Co_3O_4 replica has a highly ordered mesostructure (Fig. 3d) very similar to that of Co_3O_4-23 MPa. Figure 3e shows a HRTEM image of the sample Co_3O_4-23 MPa where the bridge between two nanorods is clearly seen. This bridge results from the filling of the interchannel micropores with Co_3O_4 [25]. It is such bridges that guarantee the connectivity of nanorods and result in the formation of highly ordered structure. At the lower pressure of 13 MPa, the precursor preferred to deposit in the main channels of the template and fewer intrawall pores were filled. Therefore, Co_3O_4-13 MPa presents randomly arranged nanorods and even isolated nanorods. However, the solvation power at the high pressure of 23 MPa was strong enough for the precursor to infiltrate into most intrawall pores, resulting in the Co_3O_4-23 MPa with a highly ordered mesoporous structure.

Figure 4 shows the nitrogen sorption isotherms of Co_3O_4-13 MPa and Co_3O_4-23 MPa. The sample Co_3O_4-23 MPa presents a type IV isotherm with a slight increase in slope at a relative pressure of ca. 0.5, followed by a sharp increase up to ca. 0.9 in both adsorption and desorption branches. The increase in slope at a relative pressure of ca. 0.5 corresponds to capillary condensation, typical of mesoporous materials with uniform pore systems, while the further increase at higher relative pressures indicates substantial interparticle porosity. The capillary condensation step is not very pronounced, indicative of relatively small sizes of ordered domains. Quite different from Co_3O_4-23 MPa, the sorption isotherm of Co_3O_4-13 MPa is featured with a sharp increase starting from $p/p_0 = 0.7$ till $p/p_0 = 1.0$, indicating the presence of large fraction of interparticle voids in accordance with the result of TEM. These large interparticle voids are expected to facilitate the mass transfer in the catalytic reactions. The pore size distributions of the two samples are illustrated in the inset of Fig. 4. The Co_3O_4-23 MPa has a rather narrow pore size distribution centered at 3.7 nm, which is in agreement with the result obtained by TEM. For the Co_3O_4-13 MPa, there are two sets of different pores in the pore size distributions, one set is uniform mesopores and centered at 3.2 nm. In combination with TEM result, we believe that this fraction of mesopores originates from small domains of orderly arranged nanorods. The other set of mesopores has a very wide pore size distribution from several nanometers to tens of nanometers, and the peak is positioned at around 23 nm. Based on the TEM result, this part of irregular mesopores is constituted of interparticle voids.

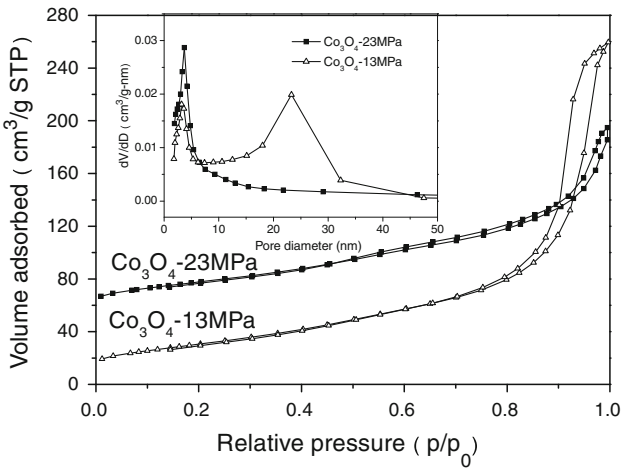

Fig. 4 Nitrogen physisorption isotherms and corresponding BJH pore size distributions for Co_3O_4-13 MPa and Co_3O_4-23 MPa. For clarity, the isotherms were offset vertically

The textural parameters of the mesoporous Co_3O_4 are summarized in Table 1. All the three mesoporous Co_3O_4 materials possess large surface areas above 100 m^2/g, whereas the bulk Co_3O_4 has only a surface area of 18 m^2/g due to the excessive growth of the crystalline particles. In particular, compared with the two ordered mesoporous Co_3O_4 materials, the randomly organized nanorod Co_3O_4 presents a larger surface area and a higher pore volume attributed to the large interparticle voids. It should be stressed that the residual silica in both mesoporous materials contributes little to the large surface areas of Co_3O_4 since it accounts for only 1.5 wt% for Co_3O_4-13 MPa and 1.7 wt% for Co_3O_4-23 MPa.

All the above characterizations on Co_3O_4 replicas demonstrate that $scCO_2$ deposition is a very effective and flexible approach for the nanocasting synthesis of mesoporous Co_3O_4 with different morphologies. What's more, the deposit of the precursor on the external surface of the template is avoided under $scCO_2$ conditions. By tuning the pressure of $scCO_2$, the pore filling percents can be altered remarkably, which then results in changes in the morphologies of the final replica. If an ordered mesoporous Co_3O_4 material is desirable, deposition at a high $scCO_2$ pressure is required. On the contrary, if randomly organized nanorods are preferred, a low $scCO_2$ pressure is enough. In the subsequent part, we will show that the different morphologies produced at different $scCO_2$ pressures result in remarkable differences in the catalytic activity for CO oxidation.

Co_3O_4 has been proven to have high catalytic activity in CO oxidation reaction [5, 26]. It is reported that the catalytic activities of the Co_3O_4 materials strongly depend on

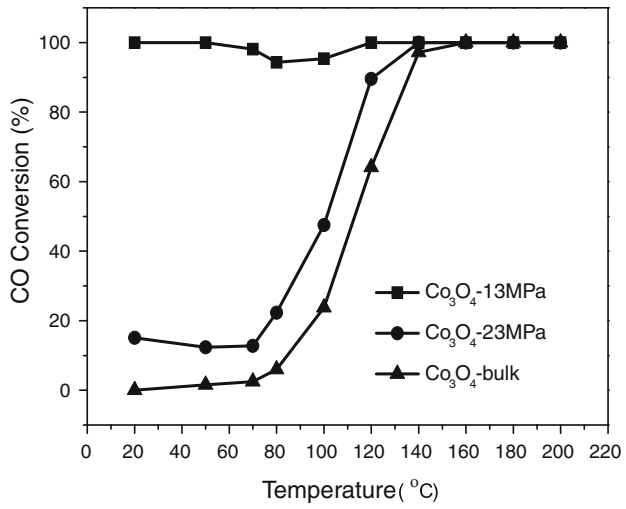

Fig. 5 CO conversions with the reaction temperature over various Co_3O_4 samples. The gas composition: 1 vol% CO, 1 vol% O_2, and 98 vol% He. Space velocity: 20 000 mL g_{cat}^{-1} s^{-1}

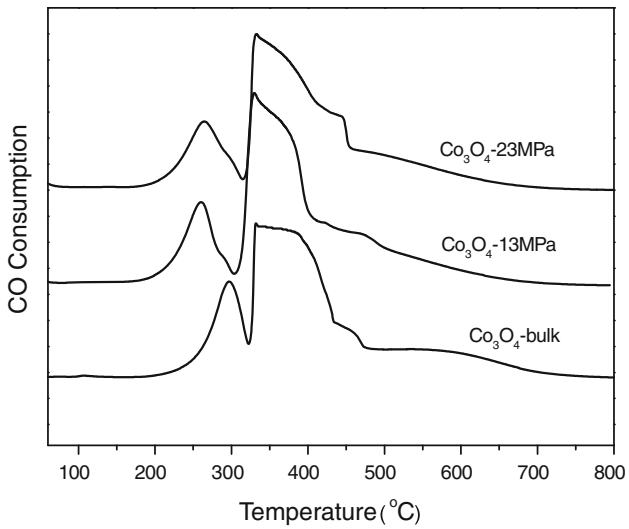

Fig. 6 CO-TPR profiles of Co_3O_4-13 MPa, Co_3O_4-23 MPa and Co_3O_4-bulk

their morphologies, crystal sizes, and exposed crystal facets [3, 4, 27]. In the present work, the catalytic performances of the meso-structured Co_3O_4 samples are evaluated using CO oxidation as a model reaction. Fig. 5 shows the CO conversion profiles as a function of the reaction temperature over different Co_3O_4 samples. The bulk Co_3O_4 did not exhibit CO conversion at room temperature. Until 80 °C the conversion of CO began to occur, and the total conversion of CO was achieved at 160 °C. On the other hand, the ordered mesoporous Co_3O_4 was only slightly more active than the bulk Co_3O_4, with the total CO conversion at 140 °C. According to the CO conversions at the reaction temperature of 80 °C, we calculated the turnover frequencies (TOFs) of the two samples, and they are 0.018 mmol m^{-2} s^{-1} for Co_3O_4-23 MPa and 0.027 mmol m^{-2} s^{-1} for Co_3O_4-bulk. Clearly, the intrinsic activity of the Co_3O_4-23 MPa based on surface area is even lower than the bulk Co_3O_4. In comparison with the two samples, the Co_3O_4-13 MPa sample with the morphology of randomly organized nanorods behaved quite differently. The CO conversion arrived at 100% even at room temperature over this sample. With a further increase of the reaction temperature, a slight drop appeared in the CO conversion curve between 50 and 120 °C, thereafter the CO conversion still restored to 100%. Such unstable behavior of mesoporous Co_3O_4 was also observed by other researches [15]. The deactivation between 50 and 120 °C can be ascribed to the carbonate species that formed at ambient temperatures and blocked active sites [28]. With the temperature increasing above 100 °C, the carbonates are decomposed and the catalyst activity is regenerated. The TOF of Co_3O_4-13 MPa at 80 °C is calculated to be 0.071 mmol m^{-2} s^{-1}, almost triples that of Co_3O_4-23 MPa and Co_3O_4-bulk. To understand the remarkably different behavior of the three catalyst samples, we performed CO-TPR experiments. As illustrated in Fig. 6, the bulk Co_3O_4 shows two reduction peaks centered at around 300 °C and 350 °C, respectively. The former is sharp and small and can be ascribed to the reduction of Co^{3+} to Co^{2+} while the latter is broad and big and can be ascribed to the reduction of Co^{2+} to Co^0 [29]. In comparison with the bulk Co_3O_4, the first peak due to the reduction of Co^{3+} to Co^{2+} shifts to a lower temperature (around 250 °C) for the two mesoporous Co_3O_4 materials. Considering that the low-temperature activity for CO oxidation is mainly correlated with the reducibility of Co^{3+} to Co^{2+}, we can expect that the two mesoporous Co_3O_4 materials should have better activities than the bulk Co_3O_4. For the Co_3O_4-13 MPa with randomly organized nanorod morphology, the case is true. However, for the Co_3O_4-23 MPa with ordered mesoporous structure, the activity is surprisingly low although its surface area and reducibility are all comparable to the Co_3O_4-13 MPa. The low activity of ordered mesoporous Co_3O_4 for CO oxidation was also observed by Tüysüz et al. who prepared cubic ordered mesoporous Co_3O_4 using KIT-6 as the hard template [30]. Possibly, the large domains of ordered mesoporous structure exert some limits on the mass transfer during the CO oxidation. On the other hand, the large voids between particles of randomly arranged nanorods facilitate the mass transfer in the reaction, thus resulting in a higher activity for CO oxidation.

4 Conclusions

In summary, we developed a highly effective method—supercritical carbon dioxide deposition, for the synthesis of

mesoporous Co_3O_4 by using SBA-15 as the hard template. The morphologies of crystalline Co_3O_4 are effectively tuned by the $scCO_2$ pressure. Highly ordered mesoporous structure is obtained at the $scCO_2$ pressure of 23 MPa while randomly organized Co_3O_4 nanorods are achieved at the $scCO_2$ pressure of 13 MPa. The two materials have large surface areas and comparable reducibility, however, their different morphologies result in quite different activities for CO oxidation. The randomly organized Co_3O_4 nanorods exhibit much higher activity for CO oxidation with the total conversion of CO even at room temperature. This superior activity may be contributed to the large voids between particles which facilitate the mass transfer in CO oxidation. We believe that the $scCO_2$ deposition method presented here can be further applied to synthesis of other transition metal oxides with tunable morphologies and catalytic performances.

Acknowledgment This work was supported by the National Natural Science Foundation of China (21173218, 21176235, and 21103173).

References

1. Royer S, Duprez D (2011) ChemCatChem 3:24
2. Qiao BT, Wang AQ, Lin J, Li L, Su DS, Zhang T (2011) Appl Catal B 105:103
3. Xie XW, Shen WJ (2009) Nanoscale 1:50
4. Xie XW, Li Y, Liu ZQ, Haruta M, Shen WJ (2009) Nature 458:746
5. Wang YZ, Zhao YX, Gao CG, Liu DS (2007) Catal Lett 116:136
6. Rivas B, Fonseca RL, González CJ, Gutiérrez-Ortiz JI (2011) J Catal 281:88
7. Yan L, Zhang XM, Ren T, Zhang HP, Wang XL, Sou JS (2002) Chem Commun 860
8. Pollard JM, Weinstock BA, Bitterwolf TE, Griffiths PR, Newbery AP, Paine JB (2008) J Catal 254:218
9. Miao SJ, Deng YQ (2001) Appl Catal B 31:L1
10. Yue WB, Zhou WZ (2007) J Mater Chem 17:4947
11. Wang YQ, Yang CM, Schmidt W, Spliethoff B, Bill E, Schüth F (2005) Adv Mater 17:53
12. Tian BZ, Liu XY, Yang HF, Xie SH, Yu CZ, Tu B, Zhao DY (2003) Adv Mater 15:1370
13. Garcia T, Agouram S, Sánchez-Royo JF, Murillo R, Mastral AM, Aranda A, Vázquez I, Dejoz A, Solsona B (2010) Appl Catal A 386:16
14. Xia YS, Dai HX, Jiang HY, Zhang L (2010) Catal Commun 11:1171
15. Ren Y, Ma Z, Qian LP, Dai S, He HY, Bruce PG (2009) Catal Lett 131:146
16. Sun SJ, Gao QM, Wang HL, Zhu JK, Guo HL (2010) Appl Catal B 97:284
17. Yang HF, Zhao DY (2005) J Mater Chem 15:1217
18. Rumplecker A, Kleitz F, Salabas EL, Schüth F (2007) Chem Mater 19:485
19. Deng JG, Zhang L, Dai HX, Xia YS, Jiang HY, Zhang H, He H (2010) J Phys Chem C 114:2694
20. Yin JZ, Xu QQ, Wang AQ (2010) Chem Eng Commun 197:627
21. Wakayama H, Itahara H, Tatsuda N, Inagaki S, Fukushima Y (2001) Chem Mater 13:2392
22. Zhao DY, Feng JL, Hou QS, Melosh N, Fredrickson GH, Chmelka BF, Stucky GD (1998) Science 279:548
23. Cháfer A, Fornari T, Berna A, Ibañez E, Reglero G (2005) J Supercrit Fluids 34:323
24. Sietsma JRA, Meeldijk JD, Breejen JP, Helder MV, Dillen AJ, Jongh PE, Jong KP (2007) Angew Chem Int Ed 46:4547
25. Ryoo R, Ko CH, Kruk M, Antochshuk V, Jaroniec M (2000) J Phys Chem B 104:11465
26. Jansson J, Palmqvist AEC, Fridell E, Skoglundh M, Österlund L, Thormählen P, Langer V (2002) J Catal 211:387
27. Ma CY, Mu Z, Li JJ, Jin YG, Cheng J, Lu GQ, Hao ZP, Qiao SZ (2010) J Am Chem Soc 132:2608
28. Jansson J, Skoglundh M, Fridell E, Thormählen P (2001) Top Catal 16/17:385
29. Lai TL, Lai YL, Lee CC, Shu YY, Wang CB (2008) Catal Today 131:105
30. Tüysüz H, Comotti M, Schüth F (2008) Chem Commun 4022